

Surpassing the Quantum Limit in Bosonic Loss Estimation without Quantum Probes

Yu Tao¹,[✉] Xinhang Li,¹ Lang Li¹, Jingzheng Huang^{1,2,3,*}, Hongjing Li,^{1,2,3} Tao Wang^{1,2,3,†},
Linjie Zhou^{1,4,‡} and Guihua Zeng^{1,2,3,5,§}


¹State Key Laboratory of Advanced Optical Communication Systems and Networks,
School of Electronic Information and Electrical Engineering, Shanghai Jiao Tong University,
Shanghai 200240, China

²Hefei National Laboratory, Hefei 230088, China

³Shanghai Research Center for Quantum Sciences, Shanghai 201315, China

⁴SJTU-Pinghu Institute of Intelligent Optoelectronics, Pinghu, 314200, China

⁵Shanghai XunTai Quantech Co., Ltd, Shanghai, 200241, China

 (Received 5 February 2024; revised 23 May 2024; accepted 2 July 2024; published 6 August 2024)

Bosonic loss estimation has an important role in quantum metrology. It was once believed that the ultimate precision of this task is restricted to the standard quantum limit if no quantum probe is involved. Nevertheless, a recent proposal showed that this limit can be surpassed by utilizing ring resonators with coherent state probe. Here, we experimentally realize the resonator-based bosonic loss estimation and verify the resonant enhancement effect. This Letter explores the advantages of resonator-based metrology and sheds light on the development of high-precision miniature sensors.

DOI: 10.1103/PhysRevLett.133.060801

Introduction—Optical energy dissipation is one of the most important phenomena in physics, which can be essentially modeled by a bosonic loss channel [1]. Estimating the transmissivity of the bosonic loss channel is of great interest for not only fundamental studies [2] but also various applications, e.g., gas sensing [3], molecular spectroscopy [4], and optical media characterization [5].

The pioneering studies of quantum bosonic loss estimation [2,6] showed that the precision using coherent state probes at fixed input energy is restricted by the standard quantum limit, which has to be beaten by quantum probes. As the optimal choice among the candidates, Fock states can achieve precision that outperforms the standard quantum limit by a factor of $(1-a)$ [7], where a^2 represents the transmissivity of the bosonic loss channel.

However, Fock states, as well as other quantum probes, are difficult to generate and fragile to noises, making it difficult to achieve the promising precision in practice [8]. Moreover, compared to classical light, the integration of quantum light remains challenging [9]. Instead of using quantum probes, it was shown that the standard quantum limit can also be surpassed by increasing the number of interactions [10]. A conventional strategy to achieve this goal is to make the probe passing through identical channels for multiple times [11–13], which is called the multipass strategy. Alternatively, this goal can also be achieved by using cavity or all-pass ring resonator [14,15], which had been

successfully applied in various kinds of ultrahigh precision sensors [16]. Especially, Ref. [15] showed that coherent-state probes in all-pass ring resonators can outperform any quantum probe single-pass strategy in absorption estimation.

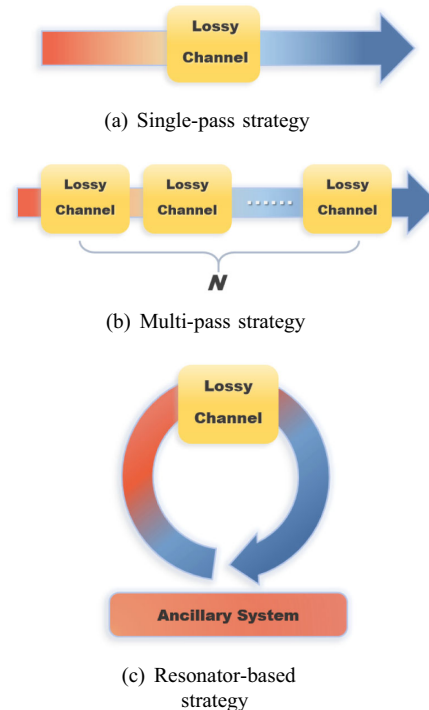


FIG. 1. The schematic diagram of bosonic loss estimation obtained by different strategies. The yellow squares represent the bosonic loss channel, which allows the target parameter, the portion a^2 of input photons to pass.

*Contact author: jzhuang1983@sjtu.edu.cn

†Contact author: tonystar@sjtu.edu.cn

‡Contact author: ljzhou@sjtu.edu.cn

§Contact author: ghzeng@sjtu.edu.cn

The logic diagrams for the resonator-based strategy in comparison with two other bosonic loss estimation strategies are, respectively, depicted in Fig. 1. In these scenarios, the lossy channel attenuates an input bosonic probe by transmitting a fraction a^2 (≤ 1) of the photons and discarding the rest. a is amplitude attenuation coefficient. For the single-pass strategy [see Fig. 1(a)], the probe interacts with the lossy channel only once. Alternatively in the multipass strategy [see Fig. 1(b)], the probe sequentially interacts with the lossy channel for N times, which leads to an N -fold improvement on precision of estimating a [17]. Obviously, multiple copies of the lossy channel must be constructed identically to promise the performance. In contrast to the above two conventional strategies, the resonator-based strategy [see Fig. 1(c)] can provide enhanced precision comparing to the single-pass strategy without lossy channel copies. In this strategy, a ring resonator working at its resonant condition is adapted to make the coherent-state probe repeatedly interact with the same lossy channel, so that the precision can be significantly improved. Under critical coupling, it can even outperform the single-pass strategy using quantum probes [15].

Principle—In theory, the precision of estimating amplitude attenuation coefficient with ν times is given by the quantum Cramér-Rao bound [18]:

$$\Delta^2 a \geq \frac{1}{\nu \mathcal{Q}(a)}, \quad (1)$$

where $\mathcal{Q}(a)$ is the quantum Fisher information (QFI). Accordingly, the optimal precision of single-pass strategy using coherent state probes can be calculated by [19]

$$(\Delta^2 a)_c = \frac{1}{4a\bar{N}_0}, \quad (2)$$

where \bar{N}_0 represents the mean photon number at the input. This bound is usually referred to the standard quantum limit. When quantum probes are allowed to be used, the optimal precision can be improved to [20]

$$(\Delta^2 a)_f = \frac{(1-a)}{4a\bar{N}_0}. \quad (3)$$

In principle, this limit can be achieved by using Fock states as input [7,20,21]. Note that the Fock states correspond to only integer photon numbers, so that one needs to engineer superpositions for arbitrary \bar{N}_0 [1]. The comparison between optimal precisions of coherent states and Fock states with the same input energy in single-pass strategy is shown in Fig. 2. In practice, Fock states face formidable challenges in application due to the low fidelity and low success probability [19,22,23].

Now let us consider the resonator-based strategy using coherent state probes, and analyze its performance with comparison to the above two cases. As depicted in Figs. 3(a) and 3(b), the bosonic loss channel refers to the ring per round with transmissivity of a^2 . In this context, a is

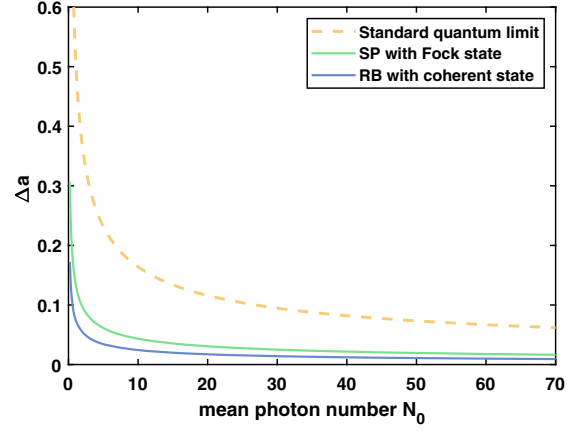


FIG. 2. The standard deviation Δa obtained by different strategies. The yellow dashed line depicts the standard quantum limits; the green line illustrates the precision limit of quantum enhancement by quantum light, which can be achieved by the Fock state in a single-pass (SP) strategy; the blue line demonstrates the precision improvement achieved by the coherent state in a resonator-based (RB) strategy. Parameters to the figure are as follows: $a = 0.93$, $r_2 = 0.99$.

also referred to as the attenuation coefficient to simplify in the ring [15,24]. The light is input to a bus waveguide and then coupled to the ring. For the add-drop type ring depicted in Fig. 3(a), part of the light is coupled out from the drop port. The transmissions corresponding to the through and drop ports are, respectively, given:

$$\eta_r = \frac{I_{\text{through}}}{I_{\text{input}}} = \frac{r_2^2 a^2 - 2r_1 r_2 a \cos \phi + r_1^2}{1 - 2r_1 r_2 a \cos \phi + (r_1 r_2 a)^2},$$

$$\eta_d = \frac{I_{\text{drop}}}{I_{\text{input}}} = \frac{(1 - r_1^2)(1 - r_2^2)a}{1 - 2r_1 r_2 a \cos \phi + (r_1 r_2 a)^2}, \quad (4)$$

where r_1 and r_2 are the self-coupling coefficients between the ring and bus waveguide up and down, respectively, and ϕ is the round-trip phase. Moreover, the phase shift imparted to the input waveguide θ_r is

$$\theta_r = \pi + \phi + \arctan \frac{r_1 \sin \phi}{a r_2 - r_1 \cos \phi} + \arctan \frac{r_1 r_2 a \sin \phi}{1 - r_1 r_2 a \cos \phi}. \quad (5)$$

The add-drop type ring can be simplified to the all-pass type when $r_2 = 1$, as is depicted in Fig. 3(b). In other words, this occurs when the straight waveguide corresponding to the drop end is not coupled to the ring, which is described in Belsley's theoretical work [15].

In consequence, the value of a can be solved from Eq. (4). The results corresponding to the add-drop and all-pass types are, respectively, shown in Fig. 3(c). While the all-pass type ring scheme suffers from value ambiguity, the add-drop type ring scheme can overcome this problem by

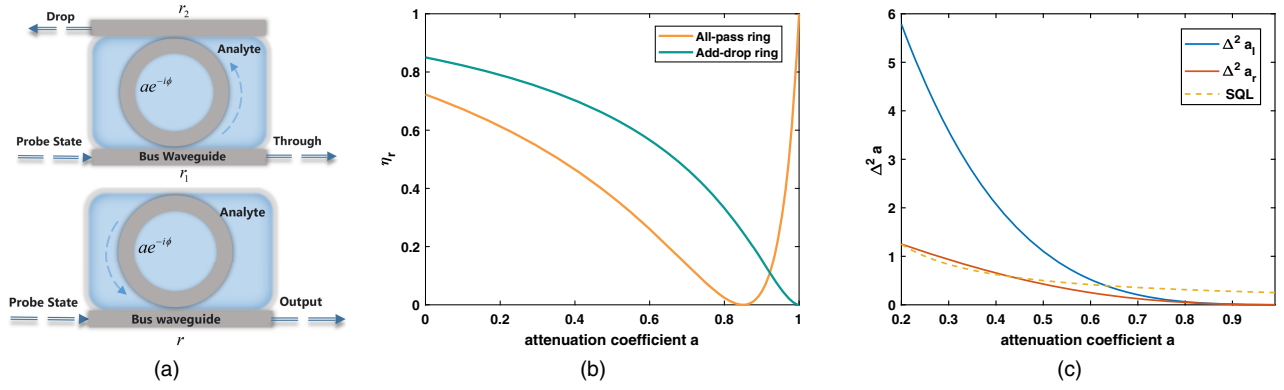


FIG. 3. (a) Two types of ring resonators: add-drop ring and all-pass ring, where the analyte can change a of the ring. (b) The relationship between the output η_r and a for various types of ring resonators. Parameters are as follows: for all pass, $r = 0.85$; for add drop, $r_1 = r_2 = 0.85$. (c) The variance of a in bosonic loss estimation normalized by the mean input photon number. Parameters for the resonator-based strategy are as follows: $r_1 = r_2 = 0.85$.

selecting appropriate r_1 and r_2 . Therefore, the add-drop type ring scheme will be adopted in the following studies.

The $Q(a)$ of any single-mode Gaussian state is given by [6]

$$Q = \frac{\text{Tr}[(\Sigma^{-1}\Sigma')^2]}{2(1+P^2)} + \frac{2P^2}{1-P^4} + \Delta\mathbf{X}'^T \Sigma^{-1} \Delta\mathbf{X}'. \quad (6)$$

The evolution of the purity is $P = \det(\Sigma)^{-1/2}$ and the rate of displacement is $\Delta\mathbf{X}' = d\langle\mathbf{X}_{a+\epsilon} - \mathbf{X}_a\rangle/d\epsilon|_{\epsilon=0}$ in phase space, where $\mathbf{X} = (\hat{x}_1, \hat{x}_2)$ and the matrix $\Sigma_{i,j} = \frac{1}{2}(\langle\hat{x}_i\hat{x}_j + \hat{x}_j\hat{x}_i\rangle - \langle\hat{x}_i\rangle\langle\hat{x}_j\rangle)$ of covariances of the quadrature operators $\hat{x}_1 = (\hat{a}^\dagger + \hat{a})$ and $\hat{x}_2 = i(\hat{a}^\dagger - \hat{a})$ [25].

An arbitrary pure single-mode Gaussian state $|\psi\rangle$ can be obtained from the vacuum state $|0\rangle$ by applying the operators of rotation \hat{R} , displacement $\hat{D}(\alpha)$, and squeezing $\hat{S}(s)$, expressed as $|\psi\rangle = \hat{R}\hat{D}\hat{S}|0\rangle$ [15,25]. For this Gaussian probe with an add-drop ring resonator, the maximum of QFI is at $r_1 = ar_2$ and $\phi = 2\pi m$, $m \in \mathbb{Z}$, given by

$$Q_G(a) = (|\alpha|^2 + \sin^2 s) \frac{4r_2^2 \eta_d}{(1 - (r_2 a)^2)(1 - r_2^2) a}. \quad (7)$$

The term $(|\alpha|^2 + \sin^2 s)$ equals to the mean photon number in this bright squeezed state.

Regarding the coherent state, which is a special case of the single-mode Gaussian state, the maximum QFI is achieved at $r_1 = ar_2$ and $\phi = 2\pi m$, $m \in \mathbb{Z}$. The maximum QFI is given by

$$Q_c(a) = |\alpha|^2 \frac{4r_2^2 \eta_d}{(1 - (r_2 a)^2)(1 - r_2^2) a}. \quad (8)$$

Note that this condition is the critical coupling and resonant condition, which is referred to the optimal operating point

in ring resonator-based strategy for achieving maximum QFI by pure single-mode Gaussian probe. Under the optimal operating point, the coherent state provides equivalent performance to that of arbitrarily bright pure single-mode squeezed probe with the same mean photon number.

Governed by Eqs. (4) and (5), the phase and loss imparted on the input bus waveguide both depend on a . The following upper bound on the QFI can be derived when estimating a [26]:

$$Q(a) \leq \bar{N}_0 \frac{4\eta_r^2 (\partial_a \theta_r)^2 + (\partial_a \eta_r)^2}{\eta_r (1 - \eta_r)} := Q_r. \quad (9)$$

Substituting η_r and θ_r into Eq. (9) yields

$$Q_r = \bar{N}_0 \frac{4r_2^2 \eta_d}{(1 - (r_2 a)^2)(1 - r_2^2) a}, \quad (10)$$

which is identical to $Q_c(a)$. In other words, the upper bound on the QFI is tight for the pure single-mode Gaussian probe in resonator-based strategy.

Therefore, when employing resonator-based strategy, the optimal precision is given by

$$(\Delta^2 a)_r = \frac{(1 - (r_2 a)^2)(1 - r_2^2) a}{4\bar{N}_0 r_2^2 \eta_d}. \quad (11)$$

It can be achieved by using coherent state. From Fig. 2, it is evident that the precision improvement based on resonator-based strategy can surpass the limits of using optimal quantum light sources in single-pass strategy.

To approach the optimal operating point, we can first employ the single-frequency laser to lock the wavelength at the resonant wavelength, satisfying the condition $\phi = 2\pi m$, $m \in \mathbb{Z}$, and then tune the coupling state to meet critical coupling condition ($a = r_1/r_2$). The corresponding a can be deduced from the optical intensity measured at the

end of the through port. In an add-drop ring, the drop port can also serve as the monitor.

The photon number variance $\langle \Delta^2 \hat{n} \rangle$ under this intensity measurement can be expressed as [15]

$$\langle \Delta^2 \hat{n} \rangle = \eta^2 \overline{\Delta^2 N_0} + \eta(1 - \eta) \overline{N_0}. \quad (12)$$

The variance in estimating a at the optimal operating point is

$$\begin{aligned} \Delta_a^2 a_I |_{r_1=r_2, \phi=2\pi m} &= \langle \Delta^2 \hat{n} \rangle \left| \frac{\partial \langle \hat{n} \rangle}{\partial a} \right|^{-2} \\ &= \frac{(1 - (r_2 a)^2)(1 - r_2^2) a}{4 \overline{N_0} r_2^2 \eta_d}, \end{aligned} \quad (13)$$

which can saturate the precision bound $(\Delta^2 a)_r$. As illustrated in Fig. 3(c), the coherent state can achieve the quantum Cramer-Rao bound at the optimal operating point with intensity measurement, being near optimal at other conditions.

The signal-to-noise ratio (SNR) at optimal operating point induced by the observable \hat{n} in the task of estimating a is defined as [27]

$$S_a[\hat{n}] = \frac{[\partial_a \langle \hat{n} \rangle]^2}{\langle \Delta^2 \hat{n} \rangle} = \frac{4 \overline{N_0} r_2^2 \eta_d}{(1 - (r_2 a)^2)(1 - r_2^2) a}, \quad (14)$$

which is the reciprocal of Eq. (13). SNR is also maximum at optimal operating point.

Experiment—To experimentally validate the resonator-based strategy, we designed and implemented an experimental setup as depicted in Fig. 4. The experiment begins with the generation of a coherent state $|\alpha\rangle$ using a single-frequency laser. This state is then directed into a multi-functional polarization controller (MPC), where we finely tune a to approach $a = r_1/r_2$. Subsequently, the light is guided towards the on-chip symmetrical racetrack-type ring resonator configured with an equal coupling coefficient, i.e., $r_1 = r_2$ for interaction. The output of the ring is measured using a homodyne detector, and the data are recorded by an oscilloscope. The through port intensity will be zero at the optimal operating point, which indicates that the probe is fully extracted by the resonator.

We alter a within the ring through the polarization control. Upon the entry of the fiber into the silicon chip, the polarization is reconfigured according to the waveguide modes supported by the chip [28]. The transmissivity of a associated with these modes exhibits different responses to changes in input polarization. Besides, different modes have different resonant wavelengths. In our experimental setup, the ring exclusively supports the fundamental modes of transverse-electric (TE) and transverse-magnetic (TM) and the input wavelength matches the resonant wavelengths of the TE mode. While maintaining the same optical

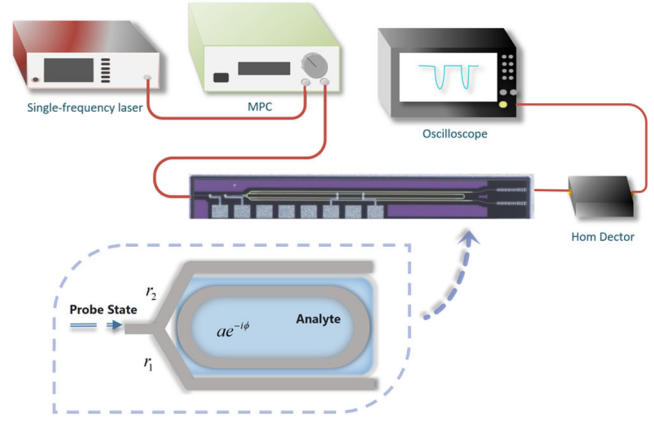


FIG. 4. Experiment setup of resonator-based strategy. The symmetrical ($r_1 = r_2$) racetrack ring resonator with attenuation coefficient a is employed to be measured. The MPC, multi-functional polarization controller, introduces the change of a within the ring. The homodyne detector is for measurement, while the oscilloscope is employed for monitoring and recording data.

intensity and slightly varying proportions of TE and TM inputs, the ring experiences changes in the overall attenuation coefficient a_{eff} due to the differential responses of TE and TM modes:

$$\begin{aligned} \eta &= (1 - b) \cdot \eta_{\text{TE}} + b \cdot \eta_{\text{TM}} \\ &= \frac{r_2^2 a_{\text{eff}}^2 - 2r_1 r_2 a_{\text{eff}} \cos \phi + r_1^2}{1 - 2r_1 r_2 a_{\text{eff}} \cos \phi + (r_1 r_2 a_{\text{eff}})^2}, \end{aligned} \quad (15)$$

where $b \rightarrow 0$, $r_1 = r_{1\text{TE}}$, $r_2 = r_{2\text{TE}}$,

$$a_{\text{eff}} = \frac{\left(1 - b + b \left(\frac{r_{2\text{TM}} a_{\text{TM}} + r_{1\text{TM}}}{1 + a_{\text{TM}} r_{1\text{TM}} r_{2\text{TM}}} \right)^2\right) a_{\text{TE}}}{1 - b + b \left(\frac{r_{2\text{TM}} a_{\text{TM}} + r_{1\text{TM}}}{1 + a_{\text{TM}} r_{1\text{TM}} r_{2\text{TM}}} \right)^2 a_{\text{TE}}^2} \quad (16)$$

(Supplemental Material, note A provides the derivation [29]).

We have also considered other effects of polarization alteration [39]: self-coupling coefficient r and the effective refractive index. On the one hand, from Eq. (15), self-coupling coefficients remain consistent with subtle changes in polarization. Additionally, the ring in our setup is a symmetrical structure with identical coupling sections. At the optimal operating point, where $a = r_2/r_1$, simultaneous variations in r_1 and r_2 can also counteract the effects of changes in the coupling coefficient. On the other hand, the shift in resonance wavelength due to changes in polarization is less than 1 pm with negligible perturbation from the optimal operating point (Supplemental Material, note E provides more details [29]).

In this proof-of-principle experiment, it is important to have precise control of the resonant wavelength. Additionally, resonators exhibit notable sensitivity to thermal fluctuations, increasing complexity to achieving stability [40]. Hence, we use a single-frequency locked

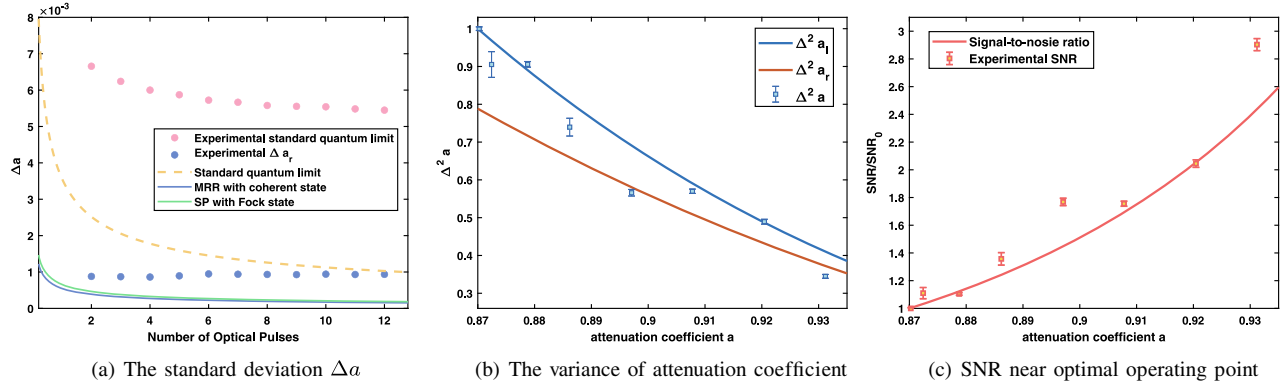


FIG. 5. The experimental results. (a) The Δa obtained by different strategies. (b) The blue line represents theoretical $\Delta^2 a$ with intensity measurement, while the blue dots represent the corresponding experimental data within this range. The red line depicts $\Delta^2 a_r$, indicating the precision bound determined by resonator-based strategy. The result normalized both experimental and theoretical data using variance achieved at $a = 0.870$ as reference. (c) The signal-to-noise ratio near the optimal operating point shows great improvement. As reference, SNR_0 refers to the SNR achieved at $a_0 = 0.870$.

laser with narrow linewidth and employ a customized miniature cooling chamber to regulate the temperature of the ring resonator, maintaining the resonant wavelength stability.

The experimental results are shown in Fig. 5. We first make resonator work at the critical operating point. In practical experiment, a is at 0.96. Keeping the input optical power constant at -25.82 dBm, with a sampling time $\tau = 1$ ns as the integration time for a single pulse, the corresponding number of photons per pulse N_τ is 2.0415×10^4 . The average number of photons is $N_0 = kN_\tau$, directly proportional to the number of optical pulses k . We increased the number of input optical pulses at different strategies and calculated the corresponding standard deviations. The result is illustrated in Fig. 5(a). Even in the presence of significant electrical noise and without fully reaching the optimal operating point, it can still be observed that the resonator-based strategy can surpass the standard quantum limit.

In Fig. 5(b), we are primarily focused on how the variance fluctuations of the measured a change near the optimal operating point. The input optical power of the system is -14.50 dBm, with the wavelength locked at 1550.0172 nm. Subsequently, a is gradually adjusted from 0.870 to 0.931, and 10 003 data points are collected in each iteration to calculate the variance. The red line represents $\Delta^2 a_r$, signifying the precision limit of resonator-based strategy. The blue line represents $\Delta^2 a_l$ in estimating a with intensity measurement, and the blue dots depict the experimental results within this range. To be clarified, both experimental and theoretical data are normalized, respectively, at $a_0 = 0.870$. It becomes evident that the variance aligns closely with the theoretical expectations over this range. Furthermore, as we approach the optimal operating point, $a = 1$, the variance with intensity measurement keeps decreasing and gradually approaches the precision limit of the resonator-based strategy.

Remarkably, we also observe that when $a \rightarrow 1$, the output light intensity gradually diminishes to zero. There is still an astonishing signal-to-noise ratio improvement as illustrated in Fig. 5(c). In experiment, the SNR at $a = 0.931$ attains a threefold enhancement compared to that at $a_0 = 0.870$.

Discussion—Here we assume resonators work in steady-state during measurement. When the speed of change in attenuation coefficient (namely, da/dt) is very slow compared to the speed of establishing steady state in the resonator, it can be considered as a slowly varying lossy channel and our approach is fast enough to measure the time-dependent losses. Typically, the response time to establish a steady state is on the order of 10^{-9} sec, or even less, which is sufficient for detecting most time-varying scenarios. Although the experimental demonstration is done for measuring losses of the ring resonator itself, the resonator-based strategy can be applied to more general scenarios. Physically, it can be implemented in various types of optical resonators, such as a Fabry-Perot cavity [30] (Supplemental Material, note B provides more details [29]). It can be employed across various physical media including optical fibers [31,32] and free space [33]. When optical resonators meet the conditions for critical coupling and resonance, our approach can be readily extended beyond integrated photonics and ring resonators.

Conclusion—In summary, we have demonstrated a proof-of-principle experiment of resonator-based strategy in bosonic loss estimation, which provides a practical way to surpass the quantum limit with coherent state. We investigate the measurement capability of the add-drop ring resonator, which can avoid ambiguity encountered with the all-pass ring. Moreover, the effect of mode perturbation and other impacts of disturbance toward the resonator are theoretically analyzed for practical purposes. Finally, the experimental resonator-based strategy presented in this Letter sheds light

on the development of compact high-precision sensors related to bosonic loss estimation [41–43].

Acknowledgments—This work was supported by the National Natural Science Foundation of China (No. 62071298, No. 62101320, No. 62135010), Innovation Program for Quantum Science and Technology (No. 2021ZD0300703), and Shanghai Municipal Science and Technology Major Project (Grant No. 2019SHZDZX01).

-
- [1] D. Braun, G. Adesso, F. Benatti, R. Floreanini, U. Marzolino, M. W. Mitchell, and S. Pirandola, *Rev. Mod. Phys.* **90**, 035006 (2018).
- [2] A. Monras and M. G. A. Paris, *Phys. Rev. Lett.* **98**, 160401 (2007).
- [3] W. Huang, Z. Zhou, Y. Cui, Z. Wang, and J. Chen, *Opt. Lett.* **47**, 4676 (2022).
- [4] A. Muraviev, D. Konnov, and K. Vodopyanov, *Sci. Rep.* **10**, 18700 (2020).
- [5] E. S. Polzik, J. Carri, and H. J. Kimble, *Phys. Rev. Lett.* **68**, 3020 (1992).
- [6] O. Pinel, P. Jian, N. Treps, C. Fabre, and D. Braun, *Phys. Rev. A* **88**, 040102(R) (2013).
- [7] G. Adesso, F. Dell’Anno, S. De Siena, F. Illuminati, and L. A. M. Souza, *Phys. Rev. A* **79**, 040305(R) (2009).
- [8] C. Weedbrook, S. Pirandola, R. García-Patrón, N. J. Cerf, T. C. Ralph, J. H. Shapiro, and S. Lloyd, *Rev. Mod. Phys.* **84**, 621 (2012).
- [9] G. Moody, L. Chang, T. J. Steiner, and J. E. Bowers, *AVS Quantum Science* **2**, 041702 (2020).
- [10] Y. Kim, S.-Y. Yoo, and Y.-H. Kim, *Phys. Rev. Lett.* **128**, 040503 (2022).
- [11] B. L. Higgins, D. W. Berry, S. D. Bartlett, H. M. Wiseman, and G. J. Pryde, *Nature (London)* **450**, 393 (2007).
- [12] P. M. Birchall, J. L. O’Brien, J. C. F. Matthews, and H. Cable, *Phys. Rev. A* **96**, 062109 (2017).
- [13] K. Lyons, J. Dressel, A. N. Jordan, J. C. Howell, and P. G. Kwiat, *Phys. Rev. Lett.* **114**, 170801 (2015).
- [14] Y.-T. Wang, J.-S. Tang, G. Hu, J. Wang, S. Yu, Z.-Q. Zhou, Z.-D. Cheng, J.-S. Xu, S.-Z. Fang, Q.-L. Wu *et al.*, *Phys. Rev. Lett.* **117**, 230801 (2016).
- [15] A. Belsley, E. J. Allen, A. Datta, and J. C. F. Matthews, *Phys. Rev. Lett.* **128**, 230501 (2022).
- [16] X. Jiang, A. J. Qavi, S. H. Huang, and L. Yang, *Matter* **3**, 371 (2020).
- [17] V. Giovannetti, S. Lloyd, and L. Maccone, *Phys. Rev. Lett.* **96**, 010401 (2006).
- [18] P. Kok and B. W. Lovett, Quantum metrology, in *Introduction to Optical Quantum Information Processing* (Cambridge University Press, Cambridge, England, 2010), pp. 421–453.
- [19] J. Sabines-Chesterking, R. Whittaker, S. K. Joshi, P. M. Birchall, P. A. Moreau, A. McMillan, H. V. Cable, J. L. O’Brien, J. G. Rarity, and J. C. F. Matthews, *Phys. Rev. Appl.* **8**, 014016 (2017).
- [20] E. J. Allen, J. Sabines-Chesterking, A. R. McMillan, S. K. Joshi, P. S. Turner, and J. C. F. Matthews, *Phys. Rev. Res.* **2**, 033243 (2020).
- [21] A. Fujiwara, *Phys. Rev. A* **70**, 012317 (2004).
- [22] C. Sayrin, I. Dotsenko, X. Zhou, B. Peaudecerf, T. Rybarczyk, S. Gleyzes, P. Rouchon, M. Mirrahimi, H. Amini, M. Brune *et al.*, *Nature (London)* **477**, 73 (2011).
- [23] M. Uria, P. Solano, and C. Hermann-Avigliano, *Phys. Rev. Lett.* **125**, 093603 (2020).
- [24] D. G. Rabus and C. Sada, Ring Resonators: Theory and Modeling, in *Integrated Ring Resonators. Springer Series in Optical Sciences* (Springer, Cham, 2020).
- [25] R. Loudon and P. L. Knight, *J. Mod. Opt.* **34**, 709 (1987).
- [26] P. M. Birchall, E. J. Allen, T. M. Stace, J. L. O’Brien, J. C. F. Matthews, and H. Cable, *Phys. Rev. Lett.* **124**, 140501 (2020).
- [27] R. Di Candia, F. Minganti, K. Petrovnin, G. Paraoanu, and S. Felicetti, *npj Quantum Inf.* **9**, 23 (2023).
- [28] R. J. Black and L. Gagnon, *Optical Waveguide Modes: Polarization, Coupling and Symmetry* (McGraw-Hill Education, New York, 2010).
- [29] See Supplemental Material at <http://link.aps.org/supplemental/10.1103/PhysRevLett.133.060801>, which includes Refs. [30–38], for additional information about the experimental methods and a detailed discussion of resonator-based strategy with Fabry-Perot cavity.
- [30] H. Pfeifer, L. Ratschbacher, J. Gallego, C. Saavedra, A. Faßbender, A. von Haaren, W. Alt, S. Hofferberth, M. Köhl, S. Linden *et al.*, *Appl. Phys. B* **128**, 29 (2022).
- [31] F. E. Seraji, *Prog. Quantum Electron.* **33**, 1 (2009).
- [32] Y. W. Huang, J. Tao, and X. G. Huang, *Sensors* **16**, 1424 (2016).
- [33] X.-W. Luo, X. Zhou, J.-S. Xu, C.-F. Li, G.-C. Guo, C. Zhang, and Z.-W. Zhou, *Nat. Commun.* **8**, 16097 (2017).
- [34] J. Ward and O. Benson, *Laser Photonics Rev.* **5**, 553 (2011).
- [35] R. Meyer, S. Ezekiel, D. W. Stowe, and V. Tekippe, *Opt. Lett.* **8**, 644 (1983).
- [36] W. Bogaerts, P. De Heyn, T. Van Vaerenbergh, K. De Vos, S. Kumar Selvaraja, T. Claes, P. Dumon, P. Bienstman, D. Van Thourhout, and R. Baets, *Laser Photonics Rev.* **6**, 47 (2012).
- [37] J. Aasi (The LIGO Scientific Collaboration), *Classical Quantum Gravity* **32**, 074001 (2015).
- [38] M. H. Bitarafan and R. G. DeCorby, *Sensors* **17**, 1748 (2017).
- [39] M. Chin, *Opt. Express* **11**, 1724 (2003).
- [40] M. R. Foreman, J. D. Swaim, and F. Vollmer, *Adv. Opt. Photonics* **7**, 168 (2015).
- [41] J. Hodgkinson and R. P. Tatam, *Meas. Sci. Technol.* **24**, 012004 (2012).
- [42] Y. Shin, A. P. Perera, J. S. Kee, J. Song, Q. Fang, G.-Q. Lo, and M. K. Park, *Sens. Actuators B* **177**, 404 (2013).
- [43] M. S. Luchansky and R. C. Bailey, *Anal. Chem.* **84**, 793 (2012).